EES Catalysis

PAPER

View Article Online
View Journal | View Issue

Cite this: *EES Catal.*, 2026, 4, 201

Structure–activity relationship in Co–N–C catalysts for multiple H_2O_2-related electrochemical reactions

Jie Yang, [ab] Lifang Chen, *[a] Xuya Zhu,[c] Wenwen Shi, [a] Mengxue Huang, [ab] Chang Liu, [ab] Ruimin Ding, *[a] Lin Gan *[c] and Xi Yin *[a]

Received 22nd July 2025,
Accepted 19th August 2025

DOI: 10.1039/d5ey00224a

rsc.li/eescatalysis

H_2O_2-related electrochemical reactions, including the two-electron oxygen reduction reaction (2e-ORR), H_2O_2 oxidation reaction (HPOR), and H_2O_2 reduction reaction (HPRR), have received significant attention for the electrosynthesis of H_2O_2 and energy storage. Understanding the complex structure–activity relationships among 2e-ORR/HPOR/HPRR and their connections is crucial for further developing highly efficient catalysts and working systems. Herein, we unveil these intricacies by employing model Co–N–C catalysts with a well-defined active site configuration (Co–$N_{4\text{-pyrrolic}}$ and Co–$N_{4\text{-pyridinic}}$) in a combined experimental and computational approach. We report the higher 2e-ORR/HPOR but lower HPRR activity of the $CoN_{4\text{-pyrrolic}}$ site than the $CoN_{4\text{-pyridinic}}$ site based on their reaction free energy landscapes remodeled considering the chemisorption steps of O_2 and H_2O_2. The results reveal that the binding free energy of *OOH (ΔG_{*OOH}) can only be utilized as a reliable descriptor for 2e-ORR/HPOR activity, but not indicative of HPRR activity, regardless of the scaling relationship of the common reaction intermediates (*OOH or *OH). The HPRR activity of CoN_4 sites strongly depends on the H_2O_2 adsorption strength and configuration. These findings provide valuable insights into the design of catalysts for H_2O_2-related electrochemical energy conversion and storage systems.

Broader context

Hydrogen peroxide (H_2O_2)-mediated electrochemical reactions—including two-electron oxygen reduction ($2e^-$-ORR), H_2O_2 oxidation (HPOR), and reduction (HPRR)—are pivotal for sustainable energy technologies, such as electrosynthesis of H_2O_2 (a green oxidant and energy carrier), direct H_2O_2 fuel cells, and regenerative energy storage systems. However, the efficiency of these interconnected reactions is fundamentally limited by the lack of universal activity descriptors and catalysts that can selectively drive target pathways while suppressing competing side reactions. Here, we decouple the structure–activity relationships of Co–N_4 single-atom catalysts with defined coordination environments (pyrrolic *vs.* pyridinic) for all three H_2O_2-related reactions. We demonstrate that the conventional descriptor (ΔG_{*OOH}) fails to predict HPRR activity, which is governed by H_2O_2 adsorption configurations and dissociation kinetics instead. This work provides design principles for on-demand catalysts tailored to specific H_2O_2 energy applications—enabling efficient H_2O_2 electrosynthesis, high-power fuel cells, and closed-loop H_2O_2-based energy storage.

1. Introduction

Hydrogen peroxide (H_2O_2)-related electrochemical reactions, including two-electron oxygen reduction reaction (2e-ORR), H_2O_2 oxidation reaction (HPOR), and H_2O_2 reduction reaction (HPRR), have received significant attention due to their key roles in H_2O_2 electrosynthesis,[1–5] fuel cells,[6–10] and energy storage systems.[11–14] These reactions often couple with each other positively or negatively, depending on their specific applications (Scheme 1). For instance, at the 2e-ORR electrode for H_2O_2 electrosynthesis, the undesired HPRR often occurs and consumes the valuable product.[15,16] Conversely, in the cathode of hydrogen fuel cells, the HPRR can convert harmful H_2O_2 into water, thereby enhancing stability and efficiency.[17,18] The 2e-ORR and its reverse reaction, HPOR, facilitate the electrochemical cycle of H_2O_2, offering potential applications in energy and hydrogen storage.[11] In the case of an H_2O_2 electrolyzer for power-to-H_2 conversion, the coupling of HPRR with HPOR at the anode reduces the H_2O_2 utilization and energy efficiency of the

[a] *State Key Laboratory of Coal Conversion, Institute of Coal Chemistry, Chinese Academy of Sciences, Taiyuan, Shanxi, 030001, China. E-mail: chenlifang@sxicc.ac.cn, dingrm@sxicc.ac.cn, xiyin@sxicc.ac.cn*
[b] *School of Chemical Engineering, University of Chinese Academy of Sciences, Beijing, 100049, China*
[c] *Tsinghua Shenzhen International Graduate School, Tsinghua University, Shenzhen, 518055, China. E-mail: lgan@sz.tsinghua.edu.cn*

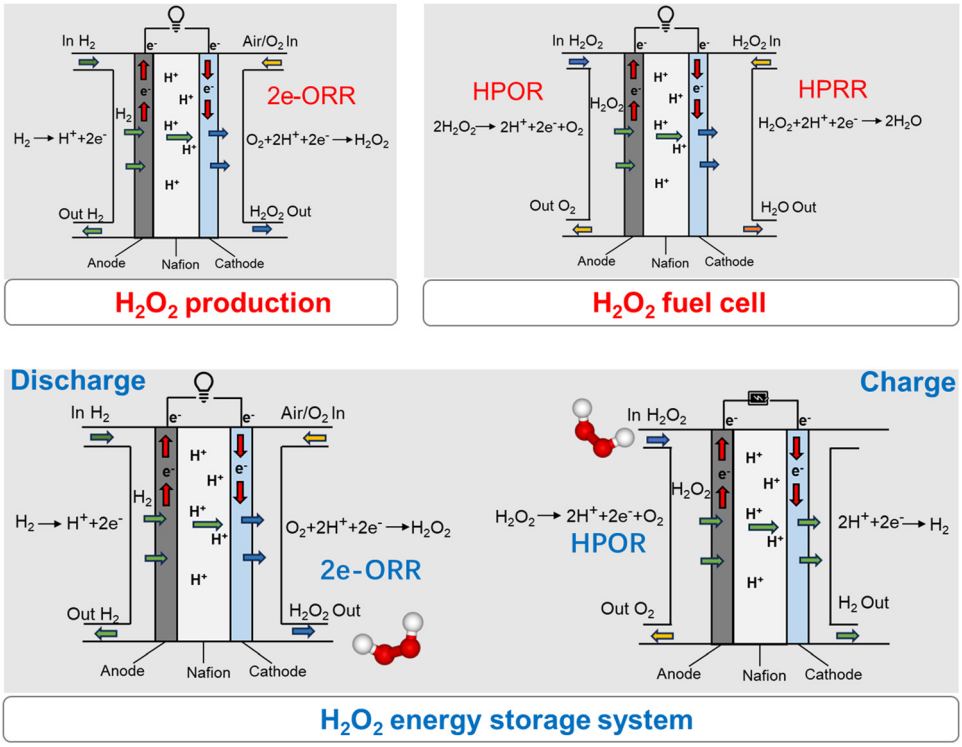

Scheme 1 Critical roles of H_2O_2-related electrochemical reactions, including 2e-ORR, HPOR, and HPRR, for various applications.

system.[13,14] Furthermore, HPOR and HPRR can be employed in driving direct-H_2O_2 fuel cells at the anode and cathode, respectively.[6–10] To date, the mechanistic studies of 2e-ORR,[2,19,20] HPOR,[11,14,21,22] and HPRR[23–26] are often conducted independently rather than being fully integrated. Given the significance of these reactions and their intricate relationships in various applications, understanding their comprehensive connections is imperative for the advancement of highly efficient catalysts and operational systems.

Among these reactions, 2e-ORR and HPOR share the same intermediate of adsorbed hydroperoxyl (*OOH, where * denotes the catalytic site), and the HPRR involves an intermediate of adsorbed hydroxyl (*OH).[2,13,27–30] The binding free energies of these intermediates, namely ΔG_{*OOH} and ΔG_{*OH}, have been proposed as the thermodynamic activity descriptors for the above reactions.[31–34] Considering the established scaling relationship between ΔG_{*OOH} and ΔG_{*OH} for various catalyst types ($\Delta G_{*OOH} = \Delta G_{*OH} + 3.2 \pm 0.2$ eV), there may be an intrinsic correlation among the 2e-ORR, HPOR, and HPRR (2e-ORR/HPOR/HPRR) processes.

Cobalt and nitrogen-doped carbon (Co–N–C), specifically those with nitrogen-coordinated cobalt (CoN_x) sites, have demonstrated activities across all three H_2O_2-related reactions.[11,15,35] For instance, Dodelet *et al.* observed that Co–N–C is a remarkable catalyst for both HPOR and HPRR,[35] and Strasser *et al.* found that Co–N–C exhibits high 2e-ORR selectivity and low HPRR activity, contributing significantly to H_2O_2 productivity.[15] However, there is a discrepancy in the HPRR activity of the Co–N–C catalyst between these findings, possibly due to differences in the coordination environment around the Co ions. A recent study combining theoretical simulation and experiments identified that pyrrolic-type CoN_4 ($CoN_{4\text{-pyrrolic}}$) is mainly responsible for the 2e-ORR, while pyridinic-type CoN_4 ($CoN_{4\text{-pyridinic}}$) catalyzes the 4e-ORR.[36] This highlights the significance of the coordination environment around Co ions for its catalytic properties. Through precise control of the coordination environment of Co, we could gain fundamental insights into the structure–activity relationship between CoN_4 and 2e-ORR/HPOR/HPRR, opening opportunities to find a correlation among these reactions.

Herein, we employ Co–N–C catalysts with $CoN_{4\text{-pyridinic}}$ and $CoN_{4\text{-pyrrolic}}$ sites to establish the structure–activity relationships for 2e-ORR/HPOR/HPRR, examining the underlying connections among these reactions. The catalyst characterization and performance evaluation confirm that the $CoN_{4\text{-pyrrolic}}$ site exhibits higher 2e-ORR and HPOR activity but lower HPRR activity compared to the $CoN_{4\text{-pyridinic}}$ site. The results from density functional theory (DFT) calculations predict the same active site structural dependency for these reactions. The chemical process involving H_2O_2 determines the HPRR activity, while ΔG_{*OOH} determines the 2e-ORR/HPRR activity. The activity of 2e-ORR and HPOR can be accurately predicted using a single thermodynamic descriptor. While HPRR follows chemical–electrochemical mechanisms, predicting its activity requires an in-depth analysis of the reaction pathway. This work advances the field by providing the first systematic investigation of three distinct H_2O_2 reaction pathways across differently coordinated CoN_4 motifs, while rigorously evaluating the universality of conventional activity descriptors through both theoretical and experimental validation. These

valuable insights into the H_2O_2-related reactions can guide the development of high-performance catalysts for various H_2O_2-based energy applications.

2. Experimental section

2.1 Materials

Cobalt chloride ($CoCl_2$, 99.7%, anhydrous, Aladdin Biochemical Technology Co.), cobalt(II) acetate tetrahydrate ($Co(CH_3COO)_2 \cdot 4H_2O$, 98%, Sigma Aldrich), zinc acetate dihydrate ($Zn(CH_3COO)_2 \cdot 2H_2O$, analytical reagent grade, Aladdin Biochemical Technology Co.), aniline (98%, Sigma-Aldrich), hydrogen peroxide (H_2O_2, 30 wt%, Alfa Aesar), 2-methylimidazole (2-MIM, $C_4H_6N_2$, 98%, Aladdin Biochemical Technology Co.), tannic acid (TA, analytical reagent grade, Aladdin Biochemical Technology Co.), hydrochloric acid (HCl, 36–38 wt%, analytical reagent grade, SCR, China), nitric acid (HNO_3, 65–68 wt%, analytical reagent grade, SCR, China), sulfuric acid (H_2SO_4, 95–98 wt%, analytical reagent grade, SCR, China), APS (98%, Sigma-Aldrich), isopropanol (IPA, >99.7%, analytical reagent grade; Kermel, SCR, China), methanol (CH_3OH, analytical reagent grade, SCR, China), deionized water (DI-water, Milli-Q, 18.2 MΩ cm at 25 °C), ultrapure N_2 (99.999%), ultrapure O_2 (99.999%), carbon black (BlackPearl 2000, Cabot Co.), 20 wt% Pt/C (Hispec3000, Johnson Matthey Co.) and a D521 Nafion dispersion (5 wt%, EW = 1100, Chemours) were utilized as received.

2.2 Preparation of catalysts

The Co–N–C catalyst, featuring $CoN_{4\text{-pyrrolic}}$ dominated coordination ($CoN_{pyrr}C$), was prepared by heating a precursor mixture containing $CoCl_2$, polymerized aniline, and oxidized carbon black (OCB). Aniline (1.024 g, 8.11 mmol) was added to 200 mL of 1 M HCl under continuous magnetic stirring to form a monomer solution. Separately, a second solution was prepared by adding 1.246 g of 30 wt% H_2O_2 solution (11 mmol H_2O_2) and 7.141 g of $CoCl_2$ (55 mmol) to 200 mL of 1 M HCl. This second solution was then introduced into the aniline solution to initiate the polymerization process. The resulting mixture was maintained at room temperature with constant magnetic stirring at 60 rpm for 4 h. Concurrently, a dispersion of OCB was prepared by sonicating 0.20 g of OCB in a mixture of 100 mL of H_2O and 10 mL of IPA. The OCB dispersion was then added to the polymer dispersion under stirring at 600 rpm. After 24 h, the combined dispersion was heated to 80 °C and concentrated under continuous stirring at 600 rpm to yield a dark slurry. Then, the slurry was loaded into an alumina combustion boat and heat-treated at 900 °C in a tube furnace in N_2 under ambient pressure. The ramping rate was 30 °C min^{-1}, and the holding time at 900 °C was 1 h. Finally, the pyrolyzed material was ground into a fine powder using an agate mortar and pestle and treated with a 12 N HCl solution for 24 h to remove spectator Co-rich phases. The acid-leached sample was washed with DI water and dried under vacuum at 60 °C. The final product was obtained after the second heat treatment at 900 °C for 3 h in flowing N_2 with a ramping rate of 30 °C min^{-1}.

$N_{pyrr}C$ refers to the blank N-doped carbon matrices that replicate the morphological features of $CoN_{pyrr}C$ but are intentionally devoid of CoN_4 coordination sites. Its synthesis follows a similar procedure to that of $CoN_{pyrr}C$ but without adding $CoCl_2$.

The Co–N–C catalyst, featuring $CoN_{4\text{-pyridinic}}$ dominated coordination ($CoN_{py}C$), was synthesized by heat treatment of the ZIF-67 material obtained by reacting acetate with 2-MIM. First, $Zn(CH_3COO)_2 \cdot 2H_2O$ (1 mmol) and $Co(CH_3COO)_2 \cdot 4H_2O$ (1 mmol) were dissolved in 5 mL of H_2O to form a clear pink solution, which was subsequently added to 5 mL of H_2O containing 2-MIM (13.6 mmol) under stirring at room temperature. The resulting mixture turned purple after a few seconds and was left undisturbed at room temperature for 4 h, then washed three times with DI water to obtain ZIF-67. Then, the prepared ZIF-67 was etched with 50 mL of TA solution (5 mg mL^{-1}) while stirring for 20 min. The products were washed with water and methanol and then dried in an oven at 80 °C. Finally, the dried powder was loaded into an alumina combustion boat and heat-treated at 900 °C (5 °C min^{-1}) in a tube furnace in N_2 at ambient pressure. The holding time at 900 °C was 2 h.

$N_{py}C$ refers to the blank N-doped carbon matrices that mimic the morphological features of $CoN_{py}C$ but lack CoN_4 coordination sites. Its synthesis is similar to that of $CoN_{py}C$ but without the incorporation of $Co(CH_3COO)_2 \cdot 4H_2O$.

2.3 Physical characterization

The Co–N–C catalysts were characterized using a scanning electron microscope (SEM, JSM-7001F, Japan) operated at an accelerating voltage of 80 kV and a high-resolution transmission electron microscope (TEM, JEM-2100F, JEOL, Japan). Powder X-ray diffraction (XRD, D8 ADVANCE A25, Bruker Co., USA) patterns were recorded using a Bruker D8-Advance-A25 diffractometer with Cu Kα radiation over a 2θ range from 5° to 90°. Raman spectra were recorded using a LabRAM HR Evolution (HORIBA Scientific, France) using a 514 nm laser as the excitation source. X-ray photoelectron spectroscopy (XPS, Axis Ultra DLD, Kratos Analytical Ltd, UK) was performed using a monochromatic Al Kα source at 150 W without charge compensation. Cobalt K-edge X-ray Co K-edge X-ray absorption spectroscopy (XAS) was measured at the XRD station of the 4B9A beamline of the Beijing Synchrotron Radiation Facility (BSRF) in the transmission or fluorescence mode.

2.4 Electrochemical measurements

The electrochemical activities of 2e-ORR were measured at ambient temperature (25 ± 2 °C) in a five-necked electrochemical cell filled with a 0.5 M H_2SO_4 electrolyte employing a bipotentiostat (CHI 760E; CH Instruments, Inc.). A rotating ring-disc electrode (RRDE, Pine Research Instrumentation) with a glassy carbon disk (Φ = 5.50 mm, area = 0.2375 cm^2) and a Pt ring was employed as the working electrode, whereas a graphite rod and reversible hydrogen electrode (RHE) were employed as the counter and reference electrodes, respectively. Catalyst ink was prepared by dispersing 5 mg of the catalyst powder in 500 μL of DI water. Subsequently, 500 μL of IPA was

added, followed by the addition of 12 μL of Nafion D521 dispersion. The mixture was then sonicated in an ice-water bath for 1 h to ensure homogeneity. Subsequently, to prepare the electrodes, 4.7 μL of the ink was deposited onto the GCE, resulting in a catalyst loading of 0.1 mg cm^{-2}. Uniform catalyst coating on the GCE was achieved by slow drying under rotation.

Their cyclic voltammograms (CVs) were recorded from 0 to 1.0 V *vs.* RHE in an N_2-saturated 0.5 M H_2SO_4 solution at a scan rate of 50 mV s^{-1}. The 2e-ORR performance was measured in O_2-saturated 0.5 M H_2SO_4 (O_2 purged for $\geq$30 min) under steady-state conditions by polarizing the working electrode from 1.0 to 0 V *vs.* RHE employing 20 mV potential steps and a hold time of 20 s at each step. The rotation rate was 900 rpm. The ring current was measured at a ring potential of 1.3 V *vs.* RHE, and the current collection coefficient of the ring electrode (N) was 0.38. The electrochemical surface areas (ECSA) of the catalyst were calculated from the equation:

$$\mathrm{ECSA} = \frac{Q}{C_s \Delta E m} \tag{1}$$

where Q is the integrated double-layer charge (mC) measured in CV over a 0–1.0 V *vs.* RHE, C_s is the specific double-layer capacitance (30 μF cm^{-2}), ΔE is the width of the potential window (1.0 V), and m is the catalyst mass loading on the electrode (mg cm^{-2}).

Electron transfer number (n) and H_2O_2 yield ($Y_{H_2O_2}$) were calculated using the following equations:

$$n = \frac{4I_d}{\left(I_d + \frac{I_r}{N}\right)} \tag{2}$$

$$Y_{H_2O_2} = 200\% \frac{\left(\frac{I_r}{N}\right)}{\left(I_d + \frac{I_r}{N}\right)} \tag{3}$$

where I_d and I_r are the disk and ring currents, respectively.

The electrochemical activities of HPOR/HPRR were measured by a bipotentiostat (CHI 760E) in an H-type electrolysis cell. A proton exchange membrane (Nafion® NR211) was used to separate the two compartments of the H-cell. A glassy carbon rotating disk electrode (RDE) (Φ = 5.00 mm, area = 0.1963 cm^2) and an Ag/AgCl (KCl, 3 M) reference electrode were placed in one cell compartment, which was filled with 0.5 M H_2SO_4 and 0.5 M H_2O_2. At the same time, a graphite rod counter electrode was positioned in the other compartment that was filled with 0.5 M H_2SO_4. Catalysts loaded at 0.1 mg cm^{-2} were prepared by depositing 3.9 μL of ink onto the GCE. CVs were recorded from 0.4 to 1.0 V *vs.* RHE in an N_2-saturated 0.5 M H_2SO_4 and 0.5 M H_2O_2 solution at a scan rate of 50 mV s^{-1}. The rotation rate was 900 rpm.

The kinetically limited current density (j_k) was determined using the Koutecký–Levich equation:

$$\frac{1}{j} = \frac{1}{j_k} + \frac{1}{j_d} \tag{4}$$

where j is the measured current density and j_d is the diffusion-limited current density.

The diffusion-limited current density is governed by the equation:

$$j_d = 0.62nFC_{H_2O_2}D_{H_2O_2}^{\frac{2}{3}}\nu^{-\frac{1}{6}}\omega^{\frac{1}{2}} \tag{5}$$

where n is the stoichiometric number of electrons transferred in the HPOR/HPRR, F is the Faraday constant, $C_{H_2O_2}$ is the concentration of dissolved H_2O_2 (0.5 M), $D_{H_2O_2}$ is the diffusion coefficient (1.3×10^{-5} cm^2 s^{-1}), ν is the kinetic viscosity of the solution (0.009 cm^2 s^{-1}), and ω is the rotation rate of the disc electrode (900 rpm).

The logarithm of the current density (j_k) was plotted against the potential to obtain a semilogarithmic polarization curve, also known as a Tafel plot. The linear part of this curve was fitted using the equation:

$$\eta = a + b \log j_k \tag{6}$$

where η is the overpotential, a is the intercept at the x-axis when $\eta = 0$, b is the Tafel slope, and j is the average of the forward and reverse scan current density in CV.

Mass activity (MA) and specific activity (SA) were quantified through the following equations:

$$\mathrm{MA} = \frac{j_k}{m} \tag{7}$$

$$\mathrm{SA} = \frac{\mathrm{MA}}{\mathrm{ECSA}} \tag{8}$$

2.5 Computational details

All spin-polarized density functional theory (DFT) calculations were performed using the GGA-PBE functional in the VASP 5.4.4 code.[37–39] The core–valence interactions were described using the projector augmented wave (PAW) pseudopotential,[40,41] with a plane-wave basis set truncated at a cut-off energy of 400 eV. The van der Waals (vdW) interactions were incorporated through the empirical Grimme's DFT-D3 method.[42] The k-point grids were set to be 4 × 4 × 1 by the Monkhorst–Pack method. Geometric optimizations employed the conjugate gradient algorithm, with force and energy convergence criteria set to 0.01 eV $Å^{-1}$ and 10^{-5} eV, respectively. A 15 Å vacuum layer was set to avoid interactions.

The chemical potential of the H^+/e^- pair is equal to half of the gas-phase H_2 at standard hydrogen electrode (SHE) conditions from the computational hydrogen electrode (CHE).[43] All free energies were calculated relative to H_2O(l) and H_2(g).

The free energy (G) for each reaction intermediate was calculated as:

$$G = E_{DFT} + \mathrm{ZPE} - TS + E_{sol} \tag{9}$$

where E_{DFT} is the total energy obtained by DFT calculations, ZPE is the zero-point energy, S is the entropy, and T is the temperature (298.15 K, in our work). For adsorbed reaction intermediates, their ZPE and S were obtained *via* vibrational frequency computations. E_{sol} is an implicit solvation correction of ~0.3 eV for the adsorption free energies.[44]

The adsorption free energies of *OOH, *OH, and *O were defined as follows:

$$\Delta G(*\mathrm{OOH}) = G(*\mathrm{OOH}) - G(*) - 2G(\mathrm{H_2O}) + 3/2G(\mathrm{H_2}) \quad (10)$$

$$\Delta G(^*\mathrm{OH}) = G(^*\mathrm{OH}) - G(^*) - G(\mathrm{H_2O}) + 1/2G(\mathrm{H_2}) \quad (11)$$

$$\Delta G(*\mathrm{O}) = G(*\mathrm{O}) - G(*) - G(\mathrm{H_2O}) + G(\mathrm{H_2}) \quad (12)$$

where ΔG(*OOH), ΔG(*OH), and ΔG(*O) are the adsorption free energies of OOH, OH, and O intermediate, respectively. G(*) is the energy of a clean surface. G(*OOH), G(*OH), and G(*O) are the free energies of intermediate (OOH, OH, and O) adsorbed on the surface. $G(\mathrm{H_2O(l)})$ and $G(\mathrm{H_2(g)})$ are the energies of free $\mathrm{H_2O(l)}$ and $\mathrm{H_2(g)}$.

3. Results and discussion

3.1 Co–N–C catalysts with $CoN_{4\text{-pyrrolic}}$ and $CoN_{4\text{-pyridinic}}$ active sites

We synthesized Co–N–C catalysts with dominant $CoN_{4\text{-pyrrolic}}$ sites ($CoN_{pyrr}C$ catalyst) and $CoN_{4\text{-pyridinic}}$ sites ($CoN_{py}C$ catalyst) using separate methods (Fig. 1a).[45,46] Briefly, the $CoN_{pyrr}C$ catalyst was prepared by heat-treatment of a precursor mixture containing cobalt(II) chloride, polyaniline (PANI), and oxidized carbon black (OCB).[45] The $CoN_{py}C$ catalyst was synthesized by heat-treatment of the ZIF-67 material obtained by reacting cobalt(II) acetate with 2-methylimidazole (2-MIM).[46]

The structural and elemental analysis results indicate that both catalysts are primarily carbon matrices doped with dispersed Co and N elements. Specifically, XRD patterns of both catalysts display a graphite-type phase, evident by two distinct characteristic peaks at 26.54° and 43.28°, corresponding to the (002) and (101) planes of graphite (PDF #75–1621), respectively (Fig. S1a). No peaks indicative of cobalt-rich phases were observed. Their Raman spectra (Fig. S1b) share a similar ratio of the D-band (disordered carbon, at *ca.* 1350 cm^{-1}) to the G-band (graphitic carbon, at *ca.* 1580 cm^{-1}) with $I_D:I_G$ ratios of 1.07 and 1.08, respectively, indicating comparable disordered graphitic structures. SEM and TEM (Fig. 1b, c and Fig. S1c, d) micrographs show that the $CoN_{pyrr}C$ catalyst exhibits an amorphous carbon particle morphology, while the $CoN_{py}C$ catalyst displays a hollow dodecahedral structure with a concave shell. EDS elemental mapping (Fig. 1d and e) indicates the distinguishable signals of C, N, and Co, revealing uniform dispersion of Co within the carbon matrix. HAADF-STEM images show

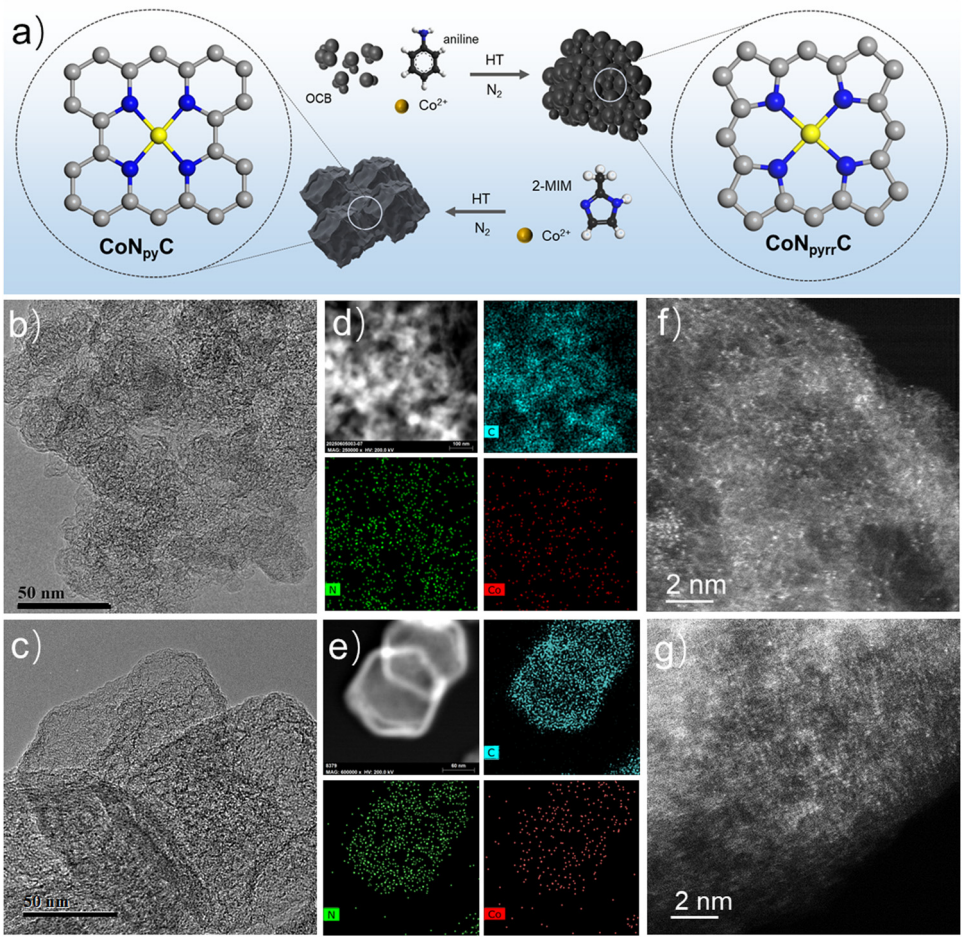

Fig. 1 (a) Schematic synthesis routes of the Co–N–C catalysts with different coordination structures. (b) and (c) TEM images; (d) and (e) elemental mapping images; and (f) and (g) HAADF-STEM images of the $CoN_{pyrr}C$ and $CoN_{py}C$ catalysts, respectively.

bright and isolated spots (Fig. 1f and g), indicative of atomically dispersed Co sites in both catalysts.

The N 1s XPS spectra of $CoN_{pyrr}C$ and $CoN_{py}C$ (Fig. 2a) can be fitted with four main types of N species, including pyridinic-N (398.6 eV), pyrrolic-N (400.3 eV), graphitic-N (401.3 eV), and oxidized-N (403.2 eV) species.[36,47,48] The fitting results (Fig. 2b and Table S1) show that the $CoN_{pyrr}C$ catalyst has a higher proportion of pyrrolic-N (*ca.* 45 at%) compared to pyridinic-N (*ca.* 22 at%). Conversely, $CoN_{py}C$ predominantly contains pyridinic-N species (*ca.* 52 at%) with a low fraction of pyrrolic-N (*ca.* 14 at%). Assuming that atomically dispersed Co is randomly coordinated with pyridinic- or pyrrolic-N sites, and considering their favorable thermodynamic formation energies,[36,49] the probability of CoN_4 sites in $CoN_{4\text{-pyrrolic}}$ or $CoN_{4\text{-pyridinic}}$ configurations is 67% *vs.* 33% in $CoN_{pyrr}C$, and 79% *vs.* 21% in the $CoN_{py}C$ catalyst.

To further investigate the oxidation state and local coordination environment of the Co ions at the atomic level, Co K-edge XAS measurements were conducted. For comparative purposes, Co foil and cobalt phthalocyanine (CoPc) were also analyzed. We acknowledge the lack of a well-defined pyridinic-CoN_4 reference material for direct XAS comparison. The Co K-edge X-ray absorption near-edge structure (XANES) spectra (Fig. 2c) show that both $CoN_{pyrr}C$ and $CoN_{py}C$ exhibit a higher pre-edge adsorption energy at the energy half of the edge maximum intensity compared to Co foil, indicating a positive valency of Co in the catalysts.[36,50,51] The XANES spectrum of CoPc shows a sharp pre-edge peak at 7712 eV (peak B), indicative of the square-planar symmetry (D_{4h}) of the CoN_4 structure (Fig. 2c).[45,47,52]

In contrast, $CoN_{pyrr}C$ and $CoN_{py}C$ lack peak B, but instead, feature a peak at 7706 eV (peak A), attributable to the distorted local structures of atomically dispersed CoN_4 sites. The presence of peak A confirms the existence of the CoN_4 site structure within the $CoN_{pyrr}C$ and $CoN_{py}C$ catalysts.

The Fourier-transform (FT) of Co K-edge extended X-ray absorption fine structure (FT-EXAFS) spectra (Fig. 2d) confirms the absence of Co–Co bonds (2.17 Å) in $CoN_{pyrr}C$ and $CoN_{py}C$, consistent with the HAADF-STEM images. The prominent peaks at 1.44 Å for $CoN_{pyrr}C$ and CoPc point to the $CoN_{4\text{-pyrrolic}}$ structure, whereas the prominent peak at 1.33 Å for $CoN_{py}C$ aligns well with the CoN_4 structures featuring a pyridinic-N configuration reported in the literature.[36,53] To further confirm this analysis, we performed a least-square curve fitting analysis for the first coordination shell of Co (Fig. S2–S5). The fitted coordination numbers for $CoN_{pyrr}C$ and $CoN_{py}C$ are 3.99 and 4.02 (Table S2), respectively, and the fitted bond lengths of Co–N in $CoN_{pyrr}C$ and $CoN_{py}C$ are 2.02 Å and 1.90 Å, respectively. These bond-length trends align with those reported by others and those from our DFT modeling (Fig. S8), validating the $CoN_{4\text{-pyrrolic}}$ and $CoN_{4\text{-pyridinic}}$ in the Co–N–C catalysts.[53,54]

The wavelet-transform (WT) of EXAFS analysis further elucidates the differences in the coordination environments across the samples, as illustrated in Fig. 2e. $CoN_{pyrr}C$ exhibits a maximum intensity around *ca.* 3.8 $Å^{-1}$, closely aligned with the Co–N path in CoPc. In contrast, $CoN_{py}C$ displays a maximum intensity at 3.6 $Å^{-1}$, reflecting its different coordination environment compared to CoN_{PyrrC}.[53] Summarizing the above results, we have experimentally obtained the Co–N–C catalysts with $CoN_{4\text{-pyridinic}}$ and $CoN_{4\text{-pyrrolic}}$ sites. These samples serve as model catalysts to explore the structure–activity relationship between the Co–N coordination structure and the ORR/HPOR/HPRR and to investigate the connections among these reactions.

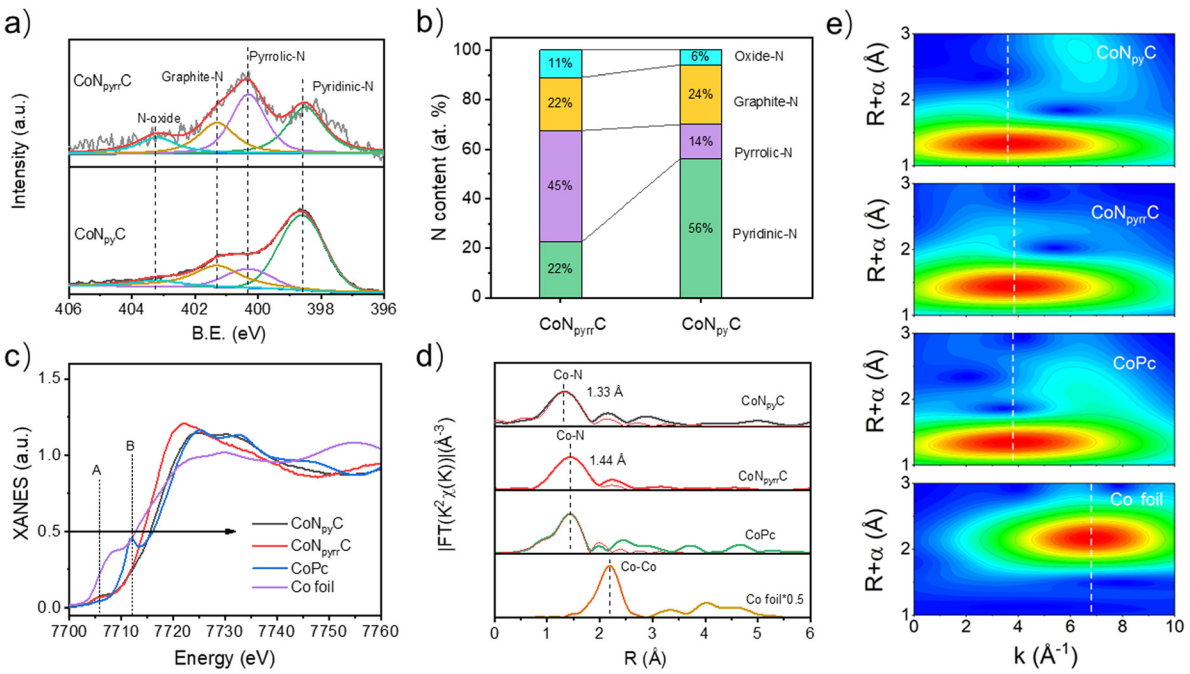

Fig. 2 (a) N 1s XPS spectra, and (b) proportion of different N species for $CoN_{pyrr}C$ and $CoN_{py}C$. (c) Co K-edge XANES spectra, (d) FT k^2-weighted and fitting EXAFS spectra, and (e) WT k^2-weighted EXAFS contour plots of the $CoN_{pyrr}C$, $CoN_{py}C$, and other reference samples.

3.2 2e-ORR/HPOR/HPRR on Co–N–C with $CoN_{4\text{-pyridinic}}$ and $CoN_{4\text{-pyrrolic}}$ sites

The Co–N–C catalysts with $CoN_{4\text{-pyridinic}}$ and $CoN_{4\text{-pyrrolic}}$ coordination exhibit distinct catalytic properties. In Fig. S6, the CV reveals comparable capacitive currents for both catalysts, corresponding to similar electrochemically active surface areas of 360.3 $m^2\ g^{-1}$ for $CoN_{pyrr}C$ and 379.8 $m^2\ g^{-1}$ for $CoN_{py}C$. This surface area equivalence establishes a controlled baseline for subsequent performance comparisons, eliminating morphological factors as primary contributors to catalytic differences. The steady-state polarization curves in Fig. 3a highlights that $CoN_{pyrr}C$ exhibits significantly higher 2e-ORR activity than $CoN_{py}C$, with an onset potential (E_{onset}) of 0.71 V *vs.* RHE, closer to the thermodynamic theoretical potential (0.695 V *vs.* RHE). The limiting current density (j_L) of $CoN_{pyrr}C$ is 2.10 mA cm^{-2}, closer to the theoretical j_L value for 2e-ORR, while that of $CoN_{py}C$ is 4.02 mA cm^{-2}. Fig. 3b compares the $Y_{H_2O_2}$ and n for these two structures. The maximum $Y_{H_2O_2}$ for $CoN_{pyrr}C$ is *ca.* 66.5% at 0.6 V *vs.* RHE, corresponding to n around 2.6. The $Y_{H_2O_2}$ for $CoN_{py}C$ is below 12% over the wide voltage range (0–0.6 V *vs.* RHE), with n close to 4. This result implies that the $CoN_{4\text{-pyrrolic}}$ coordination is more favorable for 2e-ORR than $CoN_{4\text{-pyridinic}}$ coordination.

The polarization curves of the two catalysts in an N_2-saturated solution containing 0.5 M H_2O_2 and 0.5 M H_2SO_4 electrolyte are presented in Fig. 3c. The anodic current at high potential represents the HPOR-dominated process, and the cathodic current at low potential represents the HPRR. When the anode and cathode processes are in equilibrium, the net current becomes zero at the mixing potential (U_{mix}).[11,14] For an ideal HPOR catalyst, the U_{mix} should be close to the thermodynamic equilibrium potential (0.704 V, reversible cell voltage in 0.5 M H_2SO_4 and 0.5 M H_2O_2 anolyte) to achieve high efficiency in HPOR. As displayed in Fig. 3c, $CoN_{pyrr}C$ and $CoN_{py}C$ show a U_{mix} of *ca.* 0.66 and 0.75 V *vs.* RHE. At 1.0 V *vs.* RHE, these catalysts achieve maximum current densities of *ca.* 300 and 130 mA cm^{-2}, respectively. Corresponding MA and SA at this potential, detailed in Table S3, are 5440 A g^{-1} and a SA of 1.51 mA cm^{-2} for $CoN_{pyrr}C$ *versus* 1617 A g^{-1} and 0.43 mA cm^{-2} for $CoN_{py}C$. Furthermore, the calculated Tafel slopes are 94 and 337 mV dec^{-1} for $CoN_{pyrr}C$ and $CoN_{py}C$, respectively, based on the Tafel equation (eqn (6)) (Fig. 3d). $CoN_{pyrr}C$ exhibits significantly higher HPOR activity compared to $CoN_{py}C$. We assume that the $CoN_{4\text{-pyrrolic}}$ is the active site for the HPOR process.

For the HPRR process, $CoN_{py}C$ exhibits significantly higher activity than the $CoN_{pyrr}C$ catalyst. At 0.4 V *vs.* RHE, the $CoN_{py}C$ catalyst achieves a current density of *ca.* 62 mA cm^{-2}, much higher than that of $CoN_{pyrr}C$ (*ca.* 10 mA cm^{-2}). This enhanced activity is reflected in the MA and SA values at 0.4 V *vs.* RHE. $CoN_{py}C$ achieves a markedly higher MA of 675 A g^{-1} and SA of 0.18 mA cm^{-2}, while $CoN_{pyrr}C$ displays an MA of 119.8 A g^{-1} and SA of 0.03 mA cm^{-2} (Table S3). Despite this superior activity, $CoN_{py}C$ displays a larger Tafel slope (305 mV dec^{-1}) compared to $CoN_{pyrr}C$ (231 mV dec^{-1}). It is noteworthy that

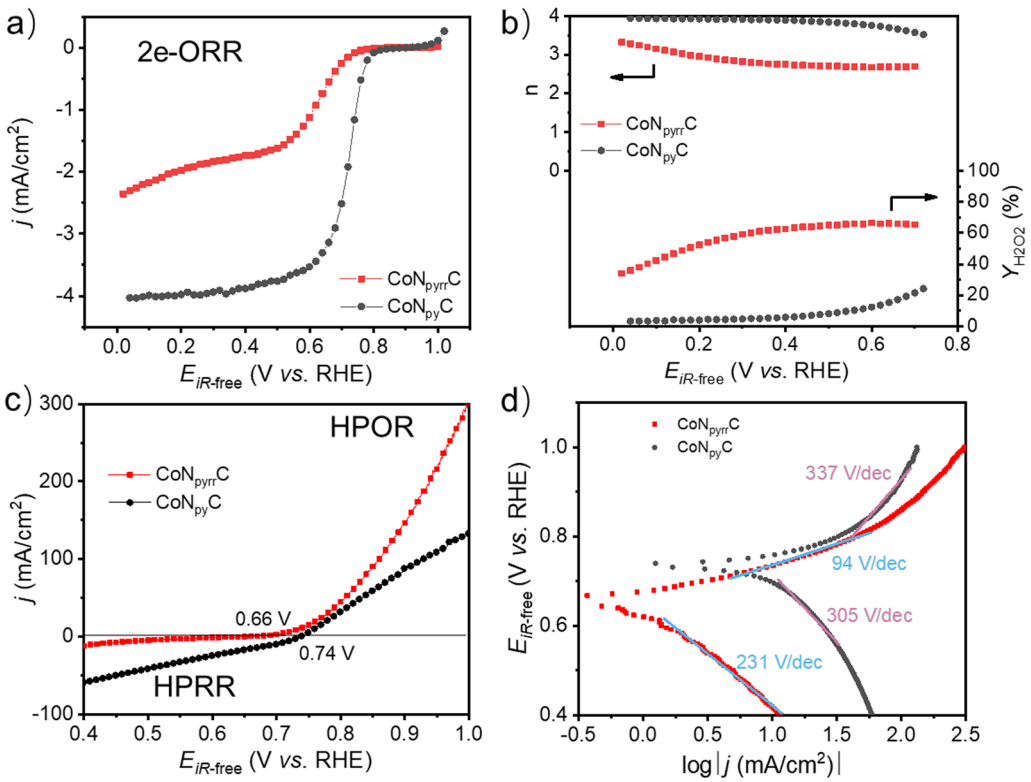

Fig. 3 (a) Steady-state ORR polarization curves, (b) $Y_{H_2O_2}$ and n in O_2-saturated 0.5 M H_2SO_4 by an RRDE system for $CoN_{pyrr}C$ and $CoN_{py}C$. (c) Polarization curves recorded at 900 rpm in N_2-saturated 0.5 M H_2SO_4 +0.5 M H_2O_2 using an H-cell system, and (d) Tafel's plot of the current density for HPOR measured with $CoN_{pyrr}C$ and $CoN_{py}C$.

both $CoN_{py}C$ and $CoN_{pyrr}C$ catalysts exhibit large Tafel slopes for the HPRR. Tafel slopes larger than 120 mV dec^{-1} are typically associated with a chemical–electrochemical mechanism in which the chemical step is rate-determining.[23] Overall, the $CoN_{4\text{-pyrrolic}}$ coordination shows high activity for 2e-ORR/HPOR, whereas $CoN_{4\text{-pyridinic}}$ coordination exhibits preferred HPRR. Critical control experiments with negligible ORR/HPOR/HPRR activity for $N_{pyrr}C$ and $N_{py}C$ blank N-doped carbon matrices (Fig. S7) further confirm that the catalytic activity difference is predominantly due to the variation in CoN_4 coordination environment rather than morphological features or residual metals.

Table S4 provides a benchmark comparison of our $CoN_{py}C$ and $CoN_{pyrr}C$ catalysts with selected CoN_4-based catalysts reported in prior studies.[15,35,55,56] It appears that the high 2e-ORR is accompanied by high HPOR and low HPRR, while when 4e-ORR occurs, it is typically accompanied by acceptable HPOR and HPRR. Subsequent DFT calculations will provide further insight into the correlation among these reactions.

3.3 Theoretical calculation on 2e-ORR/HPOR/HPRR

DFT calculations were performed to understand the structure–activity relationship between CoN_4 catalysts with $CoN_{4\text{-pyridinic}}$ and $CoN_{4\text{-pyrrolic}}$ coordination and the 2e-ORR/HPOR/HPRR. We built the $CoN_{4\text{-pyrrolic}}$ and $CoN_{4\text{-pyridinic}}$ models and optimized their structures. The optimized lattice parameters and Co–N bond length are shown in Fig. S8. The detailed calculation data for all species are displayed in Table S5.

For 2e-ORR, the generally accepted pathway in acid is as follows:[34,57]

$$* + O_2 + H^+ + e^- \rightarrow *OOH \quad (13)$$

$$*OOH + H^+ + e^- \rightarrow * + H_2O_2 \quad (14)$$

This pathway is composed of two consecutive proton-coupled electron transfer (PCET) steps, involving a single intermediate, *OOH. However, the chemisorption of oxygen ($* + O_2 \rightarrow *O_2$) and the desorption of H_2O_2 are not considered in this pathway, and the reason is not well documented.[32] Therefore, we first remodeled the 2e-ORR pathways on the $CoN_{4\text{-pyrrolic}}$ and $CoN_{4\text{-pyridinic}}$ surfaces by considering the O_2-adsorption and H_2O_2-desorption steps and compared the results with the conventional 2e-ORR pathway model. The remodeled pathway is as follows:

$$* + O_2 \rightarrow *O_2 \quad (15)$$

$$*O_2 + H^+ + e^- \rightarrow *OOH \quad (16)$$

$$*OOH + H^+ + e^- \rightarrow *H_2O_2 \quad (17)$$

$$*H_2O_2 \rightarrow H_2O_2 + * \quad (18)$$

Fig. 4a shows the reaction free energy diagrams of these pathways at U = 0.695 V. The optimized structures of the intermediates are shown in Fig. S9. We found that the strong binding of $*O_2$ at the $CoN_{4\text{-pyridinic}}$ site creates a high barrier for the next reduction step of $*O_2$ to *OOH, which would negatively affect both 4e-ORR and 2e-ORR activity (dashed line in Fig. 4a), while the slightly weak binding of $*O_2$ at the $CoN_{4\text{-pyrrolic}}$ site can be easily overcome. However, this prediction is not consistent with the observed high 4e-ORR activity of the $CoN_{py}C$ catalyst in our experiment. Alternatively, considering the O_2 gas, dissolved O_2, and $*O_2$ are at equilibrium (0.695 V) and therefore have the same chemical potential, the free energy $*O_2$ at equilibrium (rather than at the O_2 coverage used in the DFT model) can be replaced with that of free O_2. With this treatment, the conventional pathway model predicts higher 2e-ORR activity of $CoN_{4\text{-pyrrolic}}$ than $CoN_{4\text{-pyridinic}}$ (solid line in Fig. 4a). In this case, the removal of *OOH is slightly uphill, and it serves as the rate-determining step (RDS) for both $CoN_{4\text{-pyrrolic}}$ and $CoN_{4\text{-pyridinic}}$. The $CoN_{4\text{-pyrrolic}}$ exhibits a lower thermodynamic onset overpotential (η, $\eta_{2e\text{-ORR}}$ = 0.06 V) compared to the $CoN_{4\text{-pyridinic}}$ ($\eta_{2e\text{-ORR}}$ = 0.25 V), indicating that the $CoN_{4\text{-pyrrolic}}$ has a higher 2e-ORR activity than $CoN_{4\text{-pyridinic}}$.

Fig. 4b shows the volcano-type relationship between the thermodynamic limiting potential (U_L) and the binding free energy of *OOH (ΔG_{*OOH}) and the predicted values for $CoN_{4\text{-pyrrolic}}$ and $CoN_{4\text{-pyridinic}}$. The left region of the plot represents the strong binding of *OOH, while the right downhill part in the volcano plot corresponds to the weak binding of *OOH. The volcano reaches its peak at the equilibrium potential at 0.695 V with the optimal ΔG_{*OOH} of 4.225 eV. The $CoN_{4\text{-pyrrolic}}$ shows ΔG_{*OOH} of 4.16 eV, which is close to the optimal value, indicating that $CoN_{4\text{-pyrrolic}}$ prefers the 2e-ORR process. This prediction agrees with the observed low E_{onset} of 2e-ORR for the $CoN_{pyrr}C$ catalyst in Fig. 3a. Furthermore, we also investigated the electron transfer between the *OOH intermediate and these two types of CoN_4 sites by Bader charge analysis, which determines the binding strength of the *OOH intermediate. As shown in Fig. S10, the $CoN_{4\text{-pyrrolic}}$ site transfers less charge (0.28e) to the *OOH intermediate than the $CoN_{4\text{-pyridinic}}$ site (0.35e), which leads to the weaker binding of *OOH at the $CoN_{4\text{-pyrrolic}}$ site. The good agreement between the experimental and theoretical results indicates that ΔG_{*OOH} is a suitable activity descriptor for 2e-ORR at these CoN_4 sites. Therefore, deliberate engineering of $CoN_{4\text{-pyrrolic}}$ sites, guided by the ΔG_{*OOH} descriptor, provides a strategic pathway to design highly active catalysts for H_2O_2 production.

On the other hand, the HPOR is the reverse 2e-ORR process involving the same intermediate, and its pathway is as follows:

$$* + H_2O_2 \rightarrow *OOH + H^+ + e^- \quad (19)$$

$$*OOH \rightarrow * + O_2 + H^+ + e^- \quad (20)$$

Fig. 4a shows the calculated reaction free energy diagrams of the HPOR (inverse process of 2e-ORR) at 0.695 V. In the conventional pathway model, without considering the $*O_2$ and $*H_2O_2$, the RDS of HPOR for both $CoN_{4\text{-pyrrolic}}$ and $CoN_{4\text{-pyridinic}}$ is the removal of *OOH, due to the uphill energy required for converting *OOH to O_2. The $CoN_{4\text{-pyrrolic}}$ exhibits η_{HPOR} of 0.06 V, lower than 0.25 V predicted for the $CoN_{4\text{-pyridinic}}$, indicating its higher HPOR than the $CoN_{4\text{-pyridinic}}$. If considering the $*O_2$ and $*H_2O_2$ states, the model predicts O_2 desorption as the RDS for HPOR at $CoN_{4\text{-pyridinic}}$ and its lower activity than $CoN_{4\text{-pyrrolic}}$.

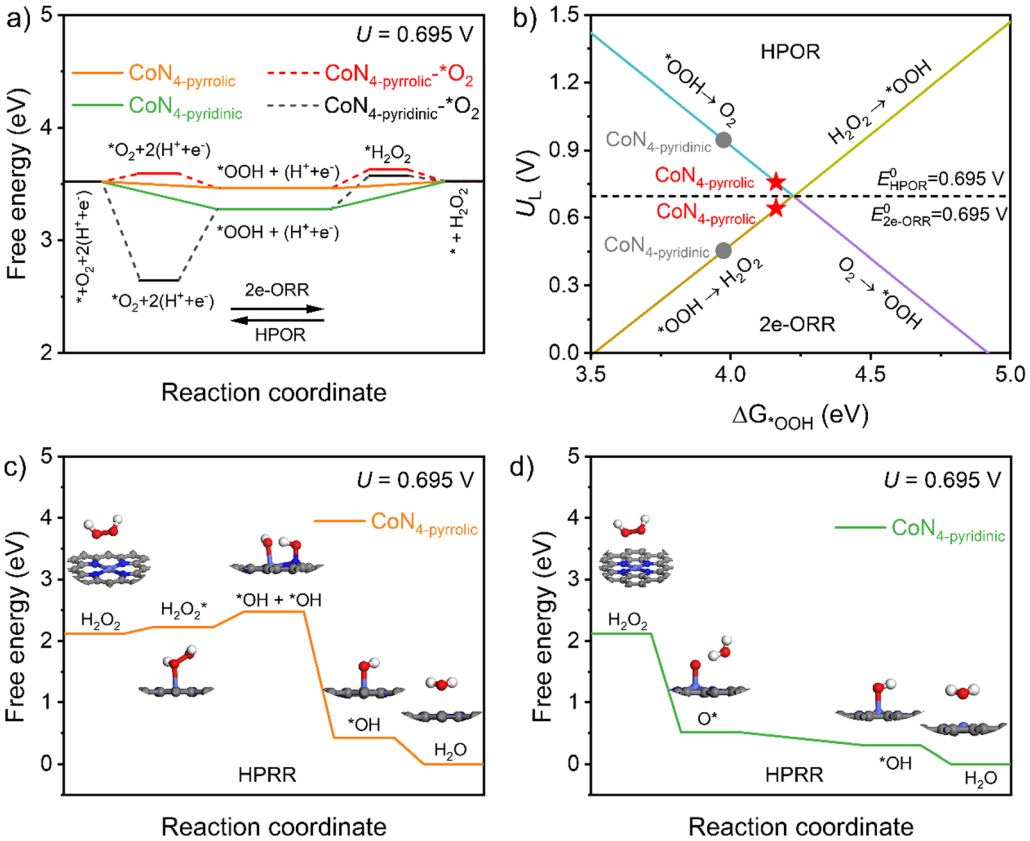

Fig. 4 (a) Free energy diagram of 2e-ORR/HPOR on the $CoN_{4\text{-pyrrolic}}$ and $CoN_{4\text{-pyridinic}}$. The dashed line represents the 2e-ORR/HPOR process including the chemisorption of reactants. (b) Volcano plot for the U_L of the 2e-ORR/HPOR against ΔG_{*OOH} on the $CoN_{4\text{-pyrrolic}}$ and $CoN_{4\text{-pyridinic}}$. (c) Free energy diagram for HPRR on the $CoN_{4\text{-pyrrolic}}$, along with the optimized structures of intermediates involved in the HPRR process on the $CoN_{4\text{-pyrrolic}}$. (d) Free energy diagram for HPRR on the $CoN_{4\text{-pyrrolic}}$, and the optimized structures of intermediates.

Fig. 4b shows the relationship between the U_L of the HPOR and ΔG_{*OOH}. An optimal HPOR catalyst should have a ΔG_{*OOH} of 4.225 eV, and the corresponding U_L should be close to the equilibrium potential (0.695 V) with minimized overpotential. The $CoN_{4\text{-pyrrolic}}$ demonstrates a ΔG_{*OOH} of 4.16 eV with a U_L of 0.76 V, which is near the theoretical equilibrium potential. While the $CoN_{4\text{-pyridinic}}$ has a ΔG_{*OOH} of 3.97 eV, and the corresponding U_L is 0.95 V. These results are consistent with the higher HPOR activity of $CoN_{pyr}C$ than $CoN_{py}C$ (Fig. 3c). Consequently, ΔG_{*OOH} serves as a thermodynamic activity descriptor for both the HPOR and 2e-ORR at CoN_4 sites. The superior HPOR and 2e-ORR demonstrated by $CoN_{4\text{-pyrrolic}}$ sites enable an efficient electrochemical cycle of H_2O_2, offering potential applications in energy and hydrogen storage.[11,13,14]

For HPRR, no general pathway has been proposed so far. The Tafel slopes observed in our results and reported for various catalysts exceed 120 mV dec^{-1}, which are very large and typical for chemical–electrochemical mechanisms.[23,58,59] Therefore, we propose the following possible chemical–electrochemical HPRR pathways on the $CoN_{4\text{-pyrrolic}}$ and $CoN_{4\text{-pyridinic}}$. On the $CoN_{4\text{-pyrrolic}}$, the HPRR is as follows:

$$* + H_2O_2 \rightarrow *H_2O_2 \quad (21)$$

$$*H_2O_2 \rightarrow *OH + *OH \quad (22)$$

$$*OH + *OH + H^+ + e^- \rightarrow *OH + H_2O \quad (23)$$

$$*OH + H^+ + e^- \rightarrow H_2O \quad (24)$$

The HPRR on the $CoN_{4\text{-pyridinic}}$ is as follows:

$$* + H_2O_2 \rightarrow *O + H_2O \quad (25)$$

$$*O + H^+ + e^- \rightarrow *OH \quad (26)$$

$$*OH + H^+ + e^- \rightarrow H_2O \quad (27)$$

where eqn (21) and (22) are the chemical pathways, eqn (23) and (24) are the electrochemical pathways on the $CoN_{4\text{-pyrrolic}}$; eqn (25) is the chemical pathway, eqn (26) and (27) are the electrochemical pathways on the $CoN_{4\text{-pyridinic}}$.

Fig. 4c and d shows the complete HPRR pathways and calculated reaction free energy diagram at $U = 0.695$ V for both $CoN_{4\text{-pyrrolic}}$ and $CoN_{4\text{-pyridinic}}$ (Fig. S11 for $U = 0$ V). On the $CoN_{4\text{-pyrrolic}}$, H_2O_2 adsorbs on top of the Co atom *via* the O atom (Fig. S12), and then dissociates to two *OH *via* HO–OH scission, which is an endothermic chemical reaction. Subsequently, these two *OH combine with two ($H^+ + e^-$) pairs to form two H_2O molecules, which is characterized by significant exothermicity. The RDS of this pathway is the HO–OH scission step, with an energy barrier exceeding 0.25 eV, in line with the chemical–electrochemical mechanism suggested by Tafel slope

analyses (Fig. 3d). In contrast, H_2O_2 undergoes spontaneous dissociation on the $CoN_{4\text{-pyridinic}}$ (Fig. S13), resulting in the formation of *O and H_2O. The *O combines with one $(H^+ + e^-)$ pair, forming *OH, followed by a second $(H^+ + e^-)$ pair and forming H_2O. This pathway is entirely exothermic, with the RDS being the electrochemical removal of *OH. Consequently, at U = 0.695 V, the HPRR activity on the $CoN_{4\text{-pyridinic}}$ is thermodynamically more favorable than that on the $CoN_{4\text{-pyrrolic}}$ surface, which aligns well with the observed activity order in Fig. 3c. Furthermore, the simple electrochemical process involving only the *OH intermediate is also calculated to compare the HPRR activity (Fig. S14). Therefore, DFT calculations and Tafel slope analysis validate the chemical–electrochemical mechanism for the HPRR on both $CoN_{4\text{-pyrrolic}}$ and $CoN_{4\text{-pyridinic}}$. This leads to the conclusion that the ΔG_{*OH} cannot serve as a reliable descriptor for HPRR. As the first atomistic-level elucidation of HPRR pathways on CoN_4 catalysts, this work provides fundamental insights for designing cathode catalysts in direct H_2O_2 fuel cells.[6–10]

It is important to note that the free energy diagram indicates that $CoN_{4\text{-pyrrolic}}$ and $CoN_{4\text{-pyridinic}}$ exhibit lower overpotentials ($\eta_{HPRR} < 0.5$ V) for HPRR, which deviates from the experimental results ($\eta_{HPRR} \approx 1$ V). This discrepancy arises from the limitations of computational methods like DFT, which focus on thermodynamics but overlook kinetic barriers crucial for reaction rates, such as proton–electron transfer. Additionally, DFT may not accurately represent realistic surface coverages of reactants or intermediates, affecting the energetics of key reaction steps. Thus, while DFT and experimental data agree on the trend that HPRR is thermodynamically favorable on $CoN_{4\text{-pyridinic}}$ surfaces, factors like reaction kinetics and surface coverage lead to higher observed overpotentials than predicted by DFT.

Our detailed theoretical investigation on $CoN_{4\text{-pyrrolic}}$ and $CoN_{4\text{-pyridinic}}$ elucidates the critical role of the *OOH intermediate as a descriptor for both the 2e-ORR and HPOR activities. The $CoN_{4\text{-pyrrolic}}$ type structure exhibits higher 2e-ORR/HPOR activity than the $CoN_{4\text{-pyridinic}}$ type structure due to its more optimal ΔG_{*OOH}. The HPRR pathway analysis offers insights that the oversimplified use of ΔG_{*OH} as a descriptor might fail to depict chemical–electrochemical mechanisms accurately. The significant differences in HPRR pathways on $CoN_{4\text{-pyrrolic}}$ and $CoN_{4\text{-pyridinic}}$ originate from H_2O_2 adsorption and thermodynamic energies. The $CoN_{4\text{-pyrrolic}}$ type structure demonstrates inferior catalytic activity in HPRR compared to the $CoN_{4\text{-pyridinic}}$ type structure, attributable to a higher chemical dissociation barrier of H_2O_2, while H_2O_2 spontaneously dissociates on the $CoN_{4\text{-pyridinic}}$. Thus, ΔG_{*OOH} can serve as a descriptor for 2e-ORR/HPOR activities, but not for the HPRR, which requires a more detailed consideration of the chemical reaction steps involved. For electrochemical H_2O_2 synthesis, we propose targeting $CoN_{4\text{-pyrrolic}}$ sites while tuning ΔG_{*OOH} toward optimal values (4.225 eV) through coordination engineering. Conversely, for H_2O_2 fuel cell cathodes requiring efficient HPRR, catalyst design should prioritize $CoN_{4\text{-pyridinic}}$ configurations that facilitate spontaneous H_2O_2 dissociation and optimize *OH binding energetics. These site-specific design principles enable the rational development of integrated systems where H_2O_2 serves as both an energy carrier (in production) and a fuel (in consumption).

4. Conclusion

We explored the intrinsic relationship between 2e-ORR/HPOR/HPRR using two model Co–N–C catalysts with CoN_4 sites in different coordination environments. The Co–N–C catalyst with $CoN_{4\text{-pyrrolic}}$ sites exhibits higher 2e-ORR and HPOR activity than that with $CoN_{4\text{-pyridinic}}$ sites, while the latter shows higher HPRR activity. Computational results indicate that the superior 2e-ORR/HPOR activity of the $CoN_{4\text{-pyrrolic}}$ site originates from its more optimal ΔG_{*OOH} value. The HPRR activity of the CoN_4 sites is determined by the chemical adsorption step of H_2O_2. The $CoN_{4\text{-pyrrolic}}$ exhibits a high H_2O_2 dissociation barrier that hinders HPRR, whereas H_2O_2 spontaneously dissociates on $CoN_{4\text{-pyridinic}}$, leading to higher HPRR activity. These results suggest that ΔG_{*OOH} can serve as a descriptor for 2e-ORR/HPOR activities, but not for the HPRR, which needs to take the chemical reaction steps into consideration. These results can provide valuable insights into the H_2O_2-related reactions and guide the development of high-performance catalysts for various H_2O_2-based energy conversion and storage applications.

Author contributions

Jie Yang: writing – original draft, methodology, investigation, and visualization. Lifang Chen: methodology, investigation, visualization, and supervision. Xuya Zhu: investigation and visualization. Wenwen Shi: investigation and visualization. Mengxue Huang: investigation and visualization. Chang Liu: investigation and visualization. Ruimin Ding: writing – review & editing, supervision, and funding acquisition. Lin Gan: writing – review & editing, supervision, and funding acquisition. Xi Yin: conceptualization, methodology, writing – review & editing, supervision, and funding acquisition.

Conflicts of interest

The authors declare no conflicts of interest.

Data availability

The data supporting this article have been included as part of the SI. See DOI: https://doi.org/10.1039/d5ey00224a.

Acknowledgements

This study was financially supported by the National Key Research and Development Program of China grant (Grant No. 2021YFB4001203), the Shanxi Province grant (Grant No. 202203021212007) and the Autonomous Research Project of SKLCC (Grant No. SCJC-HN-2023-16 and SCJC-HN-2023-17). The authors wish to thank the facility's support for the 4B9A beamline of the Beijing Synchrotron Radiation Facility (BSRF)

and the BL14W1 beamline of the Shanghai Institute of Applied Physics (SINAP).

References

1 C. Xia, Y. Xia, P. Zhu, L. Fan and H. Wang, *Science*, 2019, **366**, 226–231.
2 Z. Lu, G. Chen, S. Siahrostami, Z. Chen, K. Liu, J. Xie, L. Liao, T. Wu, D. Lin, Y. Liu, T. F. Jaramillo, J. K. Nørskov and Y. Cui, *Nat. Catal.*, 2018, **1**, 156–162.
3 H. Kim, M. Ross, N. Kornienko, L. Zhang, J. Guo, P. Yang and B. McCloskey, *Nat. Catal.*, 2018, **1**, 282–290.
4 J. Qi, Y. Du, Q. Yang, N. Jiang, J. Li, Y. Ma, Y. Ma, X. Zhao and J. Qiu, *Nat. Commun.*, 2023, **14**, 6263.
5 L. Jing, W. Wang, Q. Tian, Y. Kong, X. Ye, H. Yang, Q. Hu and C. He, *Angew. Chem., Int. Ed.*, 2024, **63**, e202403023.
6 C. J. McDonnell-Worth and D. R. MacFarlane, *Aust. J. Chem.*, 2018, **71**, 781–788.
7 Y. Yang, R. Dong, Y. Zhu, H. Li, H. Zhang, X. Fan and H. Chang, *Chem. Eng. J.*, 2020, **381**, 122749.
8 F. Yang, K. Cheng, X. Liu, S. Chang, J. Yin, C. Du, L. Du, G. Wang and D. Cao, *J. Power Sources*, 2012, **217**, 569–573.
9 A. E. Sanli and A. Aytaç, *Int. J. Hydrogen Energy*, 2011, **36**, 869–875.
10 L. An, T. Zhao, X. Yan, X. Zhou and P. Tan, *Sci. Bull.*, 2015, **60**, 55–64.
11 J. Yang, R. Ding, C. Liu, S. Liu, Q. Xu, L. Chen, J. Chen, J. Li and X. Yin, *J. Power Sources*, 2022, **545**, 231948.
12 R. Disselkamp, *Int. J. Hydrogen Energy*, 2010, **35**, 1049–1053.
13 J. Yang, R. Ding, C. Liu, L. Chen, Q. Wang, S. Liu, Q. Xu and X. Yin, *Green Chem.*, 2024, **26**, 7769–7778.
14 C. Liu, R. Ding, J. Yang, S. Liu, L. Chen, Q. Xu, J. Li and X. Yin, *ACS Sustainable Chem. Eng.*, 2023, **11**, 2599–2606.
15 Y. Sun, L. Silvioli, N. R. Sahraie, W. Ju, J. Li, A. Zitolo, S. Li, A. Bagger, L. Arnarson, X. Wang, T. Moeller, D. Bernsmeier, J. Rossmeisl, F. Jaouen and P. Strasser, *J. Am. Chem. Soc.*, 2019, **141**, 12372–12381.
16 Y. Sun, S. Li, Z. P. Jovanov, D. Bernsmeier, H. Wang, B. Paul, X. Wang, S. Kuhl and P. Strasser, *ChemSusChem*, 2018, **11**, 3388–3395.
17 C. H. Choi, H. Lim, M. Chung, G. Chon, N. Ranjbar, A. Altin, M. Sougrati, L. Stievano, H. Oh, E. Park, F. Luo, P. Strasser, G. Drazic, K. Mayrhofer, H. Kim and F. Jaouen, *Energy Environ. Sci.*, 2018, **11**, 3176–3182.
18 J. Wu, X. Yuan, J. Martin, H. Wang, J. Zhang, J. Shen, S. Wu and W. Merida, *J. Power Sources*, 2008, **184**, 104–119.
19 S. Siahrostami, A. Verdaguer, M. Karamad, D. Deiana, P. Malacrida, B. Wickman, M. Escudero, E. Paoli, R. Frydendal, T. Hansen, I. Chorkendorff, I. Stephens and J. Rossmeisl, *Nat. Mater.*, 2013, **12**, 1137–1143.
20 J. Lim, Y. Sa and S. Joo, *Cell Rep. Phys. Sci.*, 2022, **3**, 100987.
21 J. Lee, B. Lee, Y. Lee, A. Kim, D. Lee, H. Lim and H. Song, *Small*, 2023, **19**, 2303263.
22 K. Deng, W. Wang, Q. Mao, H. Yu, Z. Wang, Y. Xu, X. Li, H. Wang and L. Wang, *Small*, 2022, **18**, 2203020.
23 K. Stewart and A. Gewirth, *Langmuir*, 2007, **23**, 9911–9918.
24 V. Briega, E. Herrero and J. Feliu, *Chin. J. Catal.*, 2020, **41**, 732–738.
25 I. Katsounaros, W. Schneider, J. Meier, U. Benedikt, P. Biedermann, A. Auer and K. Mayrhofer, *Phys. Chem. Chem. Phys.*, 2012, **14**, 7384–7391.
26 R. Rizo, J. Feliu and E. Herrero, *Chin. J. Catal.*, 2021, **398**, 123–132.
27 S. Deshpande, J. Kitchin and V. Viswanathan, *ACS Catal.*, 2016, **6**, 5251–5259.
28 G. Luque, M. Rojas, G. Rivas and E. Leiva, *Electrochim. Acta*, 2010, **56**, 523–530.
29 S. Shi, J. Yang, L. Chen, M. Huang, C. Liu, R. Ding and X. Yin, *J. Electrochem. Soc.*, 2024, **171**, 046504.
30 X. Li, D. Heryadi and A. Gewirth, *Langmuir*, 2005, **21**, 9251–9259.
31 F. Calle, J. Martínez and J. Rossmeisl, *Phys. Chem. Chem. Phys.*, 2011, **13**, 15639–15643.
32 A. Kulkarni, S. Siahrostami, A. Patel and J. Nørskov, *Chem. Rev.*, 2018, **118**, 2302–2312.
33 K. Exner, *Chem. Catal.*, 2021, **1**, 258–271.
34 Z. Seh, J. Kibsgaard, C. Dickens, I. Chorkendorff, J. Nørskov and T. Jaramillo, *Science*, 2017, **355**, eaad4998.
35 F. Jaouen and J. Dodelet, *J. Phy. Chem. C*, 2009, **113**, 15422–15432.
36 S. Chen, T. Luo, X. Li, K. Chen, J. Fu, K. Liu, C. Cai, Q. Wang, H. Li, Y. Chen, C. Ma, L. Zhu, Y. Lu, T. Chan, M. Zhu, E. Cortes and M. Liu, *J. Am. Chem. Soc.*, 2022, **144**, 14505–14516.
37 J. Perdew, K. Burke and M. Ernzerhof, *Phys. Rev. Lett.*, 1996, **77**, 3865–3868.
38 G. Kresse and J. Furthmüller, *Comput. Mater. Sci.*, 1996, **6**, 15–50.
39 G. Kresse and J. Furthmüller, *Phys. Rev. B: Condens. Matter Mater. Phys.*, 1996, **54**, 11169–11186.
40 P. Blöchl, *Phys. Rev. B: Condens. Matter Mater. Phys.*, 1994, **50**, 17953–17979.
41 G. Kresse and D. Joubert, *Phys. Rev. B: Condens. Matter Mater. Phys.*, 1999, **59**, 1758–1775.
42 S. Grimme, J. Antony, S. Ehrlich and H. Krieg, *J. Chem. Phys.*, 2010, **132**, 154104.
43 J. Nørskov, J. Rossmeisl, A. Logadottir, L. Lindqvist, J. Kitchin, T. Bligaard and H. Jónsson, *J. Phys. Chem. B*, 2004, **108**, 17886–17892.
44 F. Calle-Vallejo, J. Martínez and J. Rossmeisl, *Phys. Chem. Chem. Phys.*, 2011, **13**, 15639–15643.
45 X. Yin, H. Chung, U. Martinez, L. Lin, K. Artyushkova and P. Zelenay, *J. Electrochem. Soc.*, 2019, **166**, F3240.
46 X. Ao, Y. Ding, G. Nam, L. Soule, P. Jing, B. Zhao, J. Hwang, J. Jang, C. Wang and M. Liu, *Small*, 2022, **18**, 2203326.
47 K. Artyushkova, B. Kiefer, B. Halevi, A. Knop-Gericke, R. Schlogl and P. Atanassov, *Chem. Commun.*, 2013, **49**, 2539–2541.
48 J. Wang, Y. Huang, Y. Wang, H. Deng, Y. Shi, D. Wei, M. Li, C. Dong, H. Jin, S. Mao and S. Shen, *ACS Catal.*, 2023, **13**, 2374–2385.
49 Y. Tian, M. Li, Z. Wu, Q. Sun, D. Yuan, B. Johannessen, L. Xu, Y. Wang, Y. Dou, H. Zhao and S. Zhang, *Angew. Chem., Int. Ed.*, 2022, **61**, e202213296.

50 Y. He, H. Guo, S. Hwang, X. Yang, Z. He, J. Braaten, S. Karakalos, W. Shan, M. Wang, H. Zhou, Z. Feng, K. L. More, G. Wang, D. Su, D. A. Cullen, L. Fei, S. Litster and G. Wu, *Adv. Mater.*, 2020, **32**, 2003577.
51 Y. Han, Y.-G. Wang, W. Chen, R. Xu, L. Zheng, J. Zhang, J. Luo, R.-A. Shen, Y. Zhu, W.-C. Cheong, C. Chen, Q. Peng, D. Wang and Y. Li, *J. Am. Chem. Soc.*, 2017, **139**, 17269–17272.
52 Y. Sa, S. Park, G. Jung, T. Shin, H. Jeong, S. Kwak and S. Joo, *ACS Catal.*, 2019, **9**, 83–97.
53 H. Zhuang, T. Zhang, H. Xiao, F. Zhang, P. Han, H. Gu, J. Jiao, W. Chen and Q. Gao, *Appl. Catal., B*, 2024, **340**, 123273.
54 Y. Cheng, J. Peng, G. Lai, X. Yue, F. Li, Q. Wang, L. Chen and J. Gu, *ACS Catal.*, 2024, **14**, 8446–8455.
55 J. Lee, B. Lee, Y. Lee, A. Kim, D. Lee, H. Lim and H.-K. Song, *Small*, 2023, **19**, 2303263.
56 J. Gao, H. Yang, X. Huang, S.-F. Hung, W. Cai, C. Jia, S. Miao, H. Chen, X. Yang, Y. Huang, T. Zhang and B. Liu, *Chem*, 2020, **6**, 658–674.
57 X. Sun, K. Li, C. Yin, Y. Wang, M. Jiao, F. He, X. Bai, H. Tang and Z. Wu, *Carbon*, 2016, **108**, 541–550.
58 P. Balbuena, S. Calvo, E. Lamas, P. Salazar and J. Seminario, *J. Phys. Chem. B*, 2006, **110**, 17452–17459.
59 M. Eslamibidgoli and M. Eikerling, *ACS Catal.*, 2015, **5**, 6090–6098.